Design and Implementation of a Novel Mechanical Testing System for Cellular Solids

Ara Nazarian,[1,2] Martin Stauber,[2] Ralph Müller[1,2]

[1]Orthopedic Biomechanics Laboratory, Beth Israel Deaconess Medical Center and Harvard Medical School, Boston, Massachusetts, 02215

[2]Institute for Biomedical Engineering, Swiss Federal Institute of Technology (ETH) and University of Zürich, 8044 Zürich, Switzerland

Received 5 December 2003; revised 23 October 2004; accepted 25 October 2004

Abstract: Cellular solids constitute an important class of engineering materials encompassing both man-made and natural constructs. Materials such as wood, cork, coral, and cancellous bone are examples of cellular solids. The structural analysis of cellular solid failure has been limited to 2D sections to illustrate global fracture patterns. Due to the inherent destructiveness of 2D methods, dynamic assessment of fracture progression has not been possible. Image-guided failure assessment (IGFA), a noninvasive technique to analyze 3D progressive bone failure, has been developed utilizing stepwise microcompression in combination with time-lapsed microcomputed tomographic imaging (μCT). This method allows for the assessment of fracture progression in the plastic region, where much of the structural deformation/energy absorption is encountered in a cellular solid. Therefore, the goal of this project was to design and fabricate a novel micromechanical testing system to validate the effectiveness of the stepwise IGFA technique compared to classical continuous mechanical testing, using a variety of engineered and natural cellular solids. In our analysis, we found stepwise compression to be a valid approach for IGFA with high precision and accuracy comparable to classical continuous testing. Therefore, this approach complements the conventional mechanical testing methods by providing visual insight into the failure propagation mechanisms of cellular solids.
J Biomed Mater Res Part B: Appl Biomater 73B: 400–411, 2005

Keywords: cellular solids; stepwise mechanical testing; image-guided failure assessment; cancellous bone

INTRODUCTION

Cellular solids constitute an important class of engineering materials encompassing both man-made and natural constructs. A number of underlying similarities exist between the mechanical properties of various cellular solids: for instance, the strength and stiffness of most cellular solids exhibit varying degrees of dependence on the apparent density of the construct, and the stress-strain curves generally exhibit three distinct failure phases of elastic behavior, catastrophic failure, and filling. Materials such as wood, cork, coral, and trabecular (cancellous) bone are prime examples of natural cellular solids. A number of studies have been undertaken to characterize the mechanical behavior of cancellous bone, and a number of mathematical models have been established based on the mechanics of honeycombs and foams.[1–12] Although these models tend to explain the general trends of behavior within the trabecular network, the highly variable and inhomogeneous nature of trabecular structure precludes them from determining the exact behavior of the structure.[13]

The role of apparent bone density as the most important predictor of trabecular bone mechanical strength has been thoroughly investigated.[14–18] However, the emphasis on bone density has overshadowed other important contributing factors such as trabecular microarchitecture, bone tissue properties, and loading and environmental factors. In addition, the importance of apparent bone density in predicting mechanical strength of trabecular bone is diminished as studies have shown that changes in trabecular microarchitecture lead to disproportionate changes in trabecular bone strength.[19]

Structural analysis of cellular solid failures has so far been limited to two-dimensional sections to illustrate global fracture patterns.[20–23] Due to the inherent destructiveness of the sectioning method, dynamic assessment of fracture progression has not been possible. Image-guided failure assessment (IGFA), a noninvasive technique to analyze three-dimensional progressive

---

Correspondence to: R. Müller, Institute for Biomedical Engineering, ETH and University of Zürich, Moussonstrasse 18, 8044 Zürich, Switzerland (e-mail: ralph.Mueller@biomed.ee.ethz.ch)

Contract grant sponsor: Whitaker Foundation
Contract grant sponsor: Swiss National Foundation (SNF)

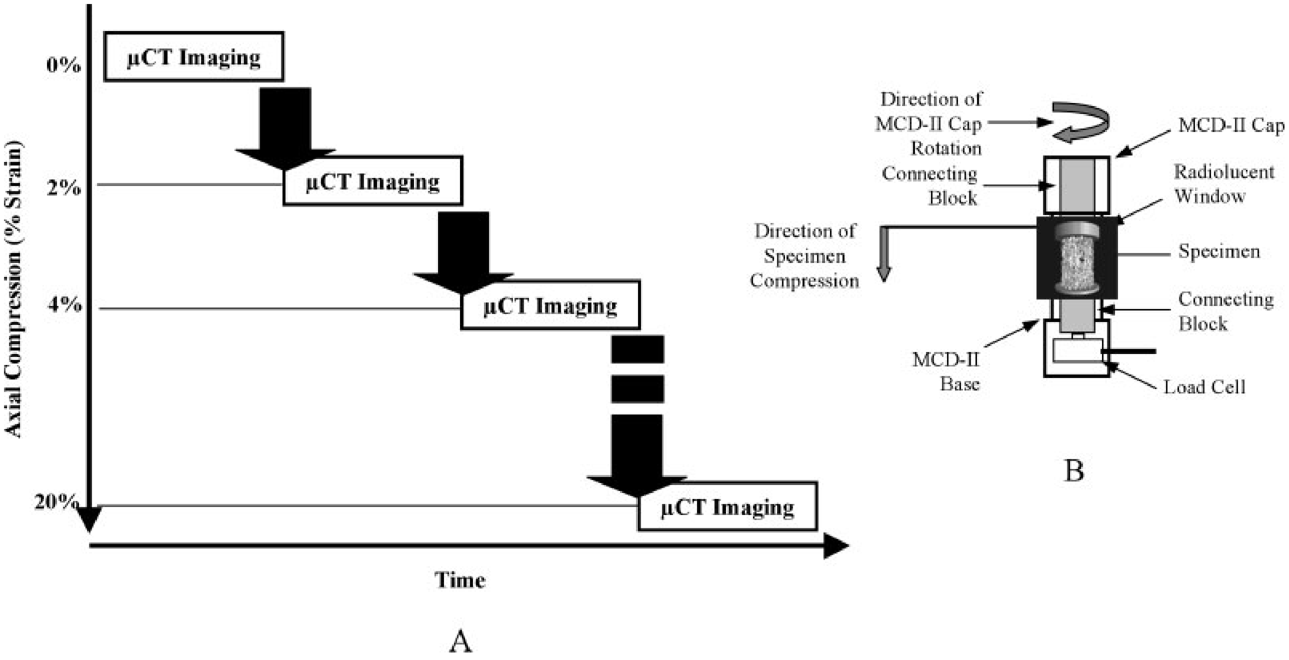

Figure 1. Schematic view of Image-Guided Failure Assessment (IGFA) technique (A) and schematic view of second generation Micro-Compression Device (MCD-II) (B).

bone failure, has been developed utilizing stepwise microcompression in combination with time-lapsed microcomputed tomographic imaging (μCT). IGFA involves the use of a microcompression device (MCD) to apply and maintain strain, and the use of μCT to image the samples in a given strain configuration.[24,25] Using the MCD and μCT, the sample is compressed and imaged in a time-lapsed fashion, allowing the assessment of fracture initiation and progression not only in the elastic region but also in the plastic region [Figure 1(A)]. In a previous study,[24] the MCD was loaded axially through a pushpin using a commercial servo-hydraulic compression device and the applied strain was locked manually. This combination introduced errors in the form of strain application fluctuation due to reduced sensitivity of the servo-hydraulic compression device at small strains and the application of unknown manual torque in the strain-locking process. Therefore, the *goal* of this project was, first, to design and fabricate a novel micromechanical testing system capable of accurately collecting the mechanical and visual failure properties of cellular solids, and, second, to observe failure behaviors of various cellular solids in order to gain insight into failure modalities involved with those solids in relation to their structural/material characteristics. This system in conjunction with the IGFA technique will provide a valuable tool to study the microarchitectural failure behavior of cellular solids in general and of cancellous bone in particular.

METHODS

Design of a Second Generation Microcompression Device (MCD-II)

The microcompression device (MCD-II) is designed to house the samples and serve as an interface between the mechanical testing and data acquisition system (MTDAQ) and the μCT scanner. Its main functions are to hold the specimen, and to translate and lock the applied strain to the sample. The dual interfacing ability of the MCD-II [Figure 1(B)] (with μCT and MTDAQ) eliminates the dependence of the testing technique on a commercial servo-hydraulic compression device. Torlon 4203, a radiolucent and stiff material (tensile, shear, and compressive strength much larger than the max applied stress in testing with minimum strain), was used to manufacture the radiolucent window capable of holding samples of 9×22 mm in size accommodating both wet and dry samples. This material was extensively tested and used for radiolucency, dimensional stability, and strength. The MCD-II serves as a suitable coupling design to interface with the MTDAQ end-effector in order to transfer strain from the end-effector to the sample. A mini button load cell, model S400 (Strain Measurement Devices, Meriden, CT) onboard the MCD-II, is connected to a data acquisition card in order to record the applied load to the sample.

Design of the Material Testing and Data Acquisition System (MTDAQ)

This system is designed to alleviate the limitations associated by using a standard servo-hydraulic compression device, where a translational linear displacement is generated from either a hydraulic or screw based system. To this end, a source of fine torque generation is employed to create a linear displacement (much like linear displacement generated by a screw rotating up or down against a frame), resulting in the application of precise strain steps and the obsolescence of the manual strain-locking process as required previously. The torque generated by a stepper motor is transmitted from the

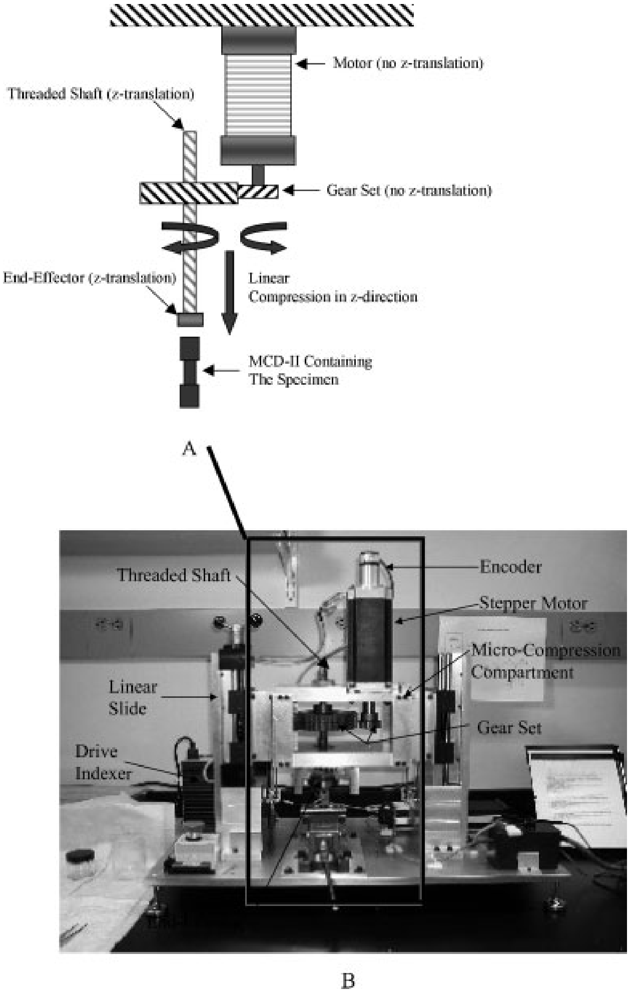

Figure 2. Schematic view of the Material Testing and Data Acquisition (MTDAQ) system (A) and detailed view of the Material Testing and Data Acquisition (MTDAQ) system with all components labeled (B).

motor to a threaded shaft via a set of gears, where it moved up and down as a result of its rotational motion [Figure 2(A)]. Power screw torque principles are employed[26] to calculate the required torque from the stepper motor to provide a maximum nominal axial force of 2,225 N. The stepper motor (HT34-438, Applied Motion Products, Watsonville, CA) provides a 15.12 Nm torque with 200 steps per revolution (1.8° per step), where it is controlled by a microstepping drive/indexer (OEMZL6104, Parker Automation, Rohnert Park, CA) capable of taking steps as small as 0.0072°. This drive/indexer is capable of maintaining position in the event of stall detection, safeguarding the position data of the MTDAQ system against mechanical failures. In addition, an encoder (755A-31-S-1000-R-HV-1-34B-10-N, Encoder Products, Sandpoint, ID) is used to create a closed loop feedback system for accurate motor position and velocity maintenance based on its quadrature incremental feedback feature. The stepper motor, drive/indexer, and the encoder communicate through Motion Architect (Parker Automation, Rohnert Park, CA) software, which is interfaced with a LabView (National Instruments, Austin, TX) environment.

The pitch of the threaded shaft and all other threaded surfaces is designed based on the overhauling principle.[26] This principle assures that the applied torque is maintained onto the sample when no displacement is applied to the sample (during imaging intervals). The end-effector, mounted at the lower end of the threaded shaft, was coupled with the MCD-II cap and transferred the applied strain to the sample. A modified vise was used to hold the MCD-II during testing, and the entire system was assembled on an aluminum base plate. The microcompression compartment was installed on a model No 252-08-10 (Nook Industries, Cleveland, OH) double shaft fully supported linear slide system on the left, and a model No 133-08-S10 slide on the right. The mounting and unmounting of the MCD-II from MTDAQ was made possible by using the above slides to lift up the MTDAQ microcompression compartment.

A linear variable differential transformer (LVDT) was attached to the end effector to monitor the displacement of the end effector and, thus, the displacement of the sample. It is noteworthy to mention that the LVDT measures the total strain including the sample strain and the load frame compliance (which is characterized independently via μCT imaging). The 100MHR LVDT (Schaevitz Sensors, Hampton, VA) with a nominal linear range of ± 2.54 mm, linearity of 0.15% of the full range (± 3.8 μm), and sensitivity of 110 mV out/V in/mm (± 962 mV) was connected to an ATA 2001 conditioner (Lucas Control Systems, Hampton, VA) for signal amplification. Figure 2(B) shows a detailed view of the MTDAQ system with labels identifying all crucial components.

Data Acquisition and Calibration of the MTDAQ and MCD-II

A PCI data acquisition card (PCI-MIO-16-E4, National Instruments, Austin, TX) with a 250 K-Samples/s sampling rate, 8 differential input channels, and 12-bit resolution was used to receive the load and displacement signals. A number of LabView (National Instruments) programs were written to control the stepper motor motion and data acquisition aspects of the system. The load cell within the MCD-II was calibrated using a previously calibrated load cell on board a servo-hydraulic mechanical testing device (Model 8511, Instron Corp., Canton, MA). The LVDT was calibrated using a high precision digital indicator (Digimatic, Mitotoyo Corp., Kawasaki, Kanagawa, Japan) installed under the MTDAQ end-effector. The results of the calibration showed highly linear correlations with a high coefficient of determination ($r^2 = 1.0$) for both the load cell and the LVDT readings.

Materials

Several engineered and biological cellular solids were used for validation of the testing system/technique. The engineered materials consisted of Duocel aluminum foams (AL) of varying relative densities, and Reticulated Silicon Carbide Ceramic (SiC) all from ERG Materials and Aerospace Corporation (Oakland, CA). The Duocel AL foam has a reticulated structure of open, duodecahedronal-shaped cells connected by solid metal trabeculae. These trabeculae routinely test to

TABLE I. Dimensions, Geometry, and Quantity of All Samples

Group	Symbol	Quantity [SW + Cont.]	Geometry	Dia [mm]	Height [mm]
4% Aluminum	AL-04	5 + 5	Cylinder	8.00	16.00
8% Aluminum	AL-08	5 + 5	Cylinder	8.00	16.00
12% Aluminum	AL-12	5 + 5	Cylinder	8.00	16.00
Silicon carbide	SiC	3 + 3	Square rod	8.24	16.80
Whale bone	WH-T	7 + 7	Cylinder	8.00	16.00
Human bone	HU-T	7 + 7	Cylinder	8.00	12.00

99% purity of the parent alloy, which for this experiment is 6101-T6 aluminum. We used AL foams of 4, 8, and 12% relative densities with an approximate pores/cm range of 15–45 (AL-04, AL-08, and AL-12). Aluminum foam is typically used in the design of heat sinks, heat exchangers, aircraft wing structures, porous electrodes, and energy absorbers for auto bumpers. It has also been used in applications by orthopedic research groups, due to its morphologic similarity to human vertebral trabecular structures. The SiC is a porous, open cell structure comprised of a 3D latticework of interconnected ceramic trabeculae with a regularly repeating pattern of cells and trabeculae. This characteristic gives the SiC its uniform material characteristics of high volume, high surface area, low flow resistance, high strength, low weight to volume ratio, thermal shock resistance and high thermal and electrical conductivity. The relative density of the SiC foam samples was approximately 8% with approximate porosity of 16 pores/cm. Please refer to Table I for the dimension, geometry, and quantity of all samples.

For biological samples, a group of bowhead whale vertebral cancellous bone samples (WH-T) and a group of human vertebral cancellous bone samples (HU-T) were selected. The whale cancellous bone samples were cored from one vertebral body, and the human trabecular samples were cored from vertebral bodies harvested from 2 cadaveric spines (65 y/o M, 63 y/o F). Due to the large size of the whale vertebral body (400 mm in diameter and 200 mm in height) and the large regions of highly homogenous, uniformly oriented cancellous bone, these vertebral bodies are ideal for acquiring a relatively large batch of samples with similar trabecular architecture and density. Human vertebral bodies typically show a much higher variation in cancellous bone structure and density due to their relatively small size and the considerable disparity in bone architecture between humans. All biological samples were preserved in saline-soaked gauze at a temperature of −20°C. The whale and human bone samples were cored parallel to the anatomical axis out of a precut block of the vertebral body using a diamond coring-tool (Starlite Industries, Rosemont, PA) while completely submerged in 0.9% saline solution. The same configurations were used to cut SiC samples, while the AL foam samples were cored and cut at the ERG facilities. Please refer to Table I for a complete listing of all sample dimension, geometry, and quantity.

Once cored, the two ends of all the cored samples were cut perpendicular to the anatomical axis of the trabeculae between two parallel diamond wafering blades running on a low-speed saw (Isomet, Buehler Corp., Lake Bluff, IL) operating under copious irrigation. These precautionary measures were taken in order to minimize the disruption of the porous network, thereby minimizing the damage artifacts at both ends of the sample and maintaining full hydration during all stages of preparation. The samples were cored and cut in accordance with recommendations for testing porous samples using a 2:1 ratio between length and diameter.[27] In the case of human cancellous bone samples, this ratio was not strictly enforced, due to the smaller size (height) of human vertebral bodies. Before testing, prealigned brass end caps with a 9-mm diameter and 1.2-mm thickness were glued with cyanoacrylate (American Glue Corp., Taylor, MI) to both ends of the samples. This step effectively reduced end artifacts[28] by restraining displacement at either end of the sample and providing support to the free ends of the unsupported elements. The biological samples remained wet during testing with the humidity sealed within the microcompression device. This was verified upon retrieval of wet samples at the end of testing periods.

Validation of the MTDAQ

A comprehensive validation study involving the above-mentioned engineered and biological cellular solids was performed to assess the reproducibility and accuracy of the results obtained from the new testing system/technique for all material types described in Materials (please refer to Table I for detailed description of sample groups). Due to the rate-dependent properties of bone and other cellular solids, stress relaxation, due to the discrete nature of the stepwise testing method, was a factor of concern with respect to the validity of the method. In order to address these concerns and prove the validity of the stepwise testing method, the results of this method were compared to those obtained from a conventional continuous test (considered to be the gold standard for the stepwise compressive mechanical testing) performed using the MTDAQ system over the same total strain range and testing conditions. To do so, samples from each foam type were randomly assigned to two subgroups of equal sample quantities. Each sub-group was then designated for either stepwise (SW) or continuous (Cont) testing, respectively. The subgroups within each foam type were selected in a manner that no inter-subgroup statistical differences were observed between the weight and apparent densities of the samples. In other words, the samples in one subgroup were very similar to those in the other subgroup of the same foam type. This arrangement allowed for comparison of the mechanical testing results obtained from stepwise testing to those obtained via conventional continuous mechanical testing using two sets of similar samples. All samples were preconditioned using the MCD-II and the MTDAQ testing systems to eliminate typical toe behavior.[29] The preconditioning was performed via a triangular waveform from 0.0 to 0.3% and back to 0% strain at a rate of 0.005 s^{-1} for 7 cycles. Then, the samples in the continuous testing groups were compressed from 0 to 20% strain at a strain rate of 0.01 s^{-1} using the MCD-II in combination with the MTDAQ. In the meantime, the samples in the stepwise testing group were transferred to the μCT for initial imaging of the sample in the intact state (0%). After imaging, the sample was returned to the MTDAQ, and exposed to a monocyclic nominal strain of 2%. Following the application of each strain step, the sample within the MCD-II was left to relax for 20 min prior to the next μCT imaging. The 20-min time interval was necessary to allow for adequate stress relaxation in the foam due to its viscoelastic material properties. This procedure was repeated five more times to acquire additional time-lapsed images at 4, 8, 12, 16, and 20% nominal strain in the postfailure regime [Figure 1(A)]. Each imaging step lasted approximately 60 to 90 min, depending on the size of the sample.

In addition to comparing results obtained from the stepwise testing method with those obtained from the conventional continuous testing method, the MTDAQ was validated by comparing our continuous test results to the mechanical test results and analytical solutions reported by other groups for the same material types and similar testing parameters.

Data Reconstruction and Analysis

The stepwise stress-strain graphs consisted of six discrete sections between the seven strain steps of 0, 2, 4, 8, 12, 16, and 20% global strain. These discontinuities did not pose any problems for cellular solids consisting of nonviscoelastic material, as issues such as stress relaxation are irrelevant. However, for cellular solids, such as bone, where there is a significant stress relaxation component due to its inherent viscoelastic nature, these discontinuities/drops in stress values present a data analysis problem. In order to address these drops and obtain a continuous load-displacement curve, the end point of the discrete section was connected to the beginning point of the next discrete section via a straight line (dashed lines in Figure 3), based on the assumption that the results obtained from the reconstructed stepwise tests would be compatible with those obtained from continuous tests. In other words, we connected a straight line from the end of one discrete displacement step to the beginning of the next discrete displacement step (Figure 3). This measure was an arbitrary method of generating continuous graphs from the stepwise data considered to be a part of our overall IGFA technique. We used the validation results to address whether the addition of these lines would give rise to a method (stepwise) capable of accurately reflecting the mechanical properties of the samples established by conventional continuous tests.

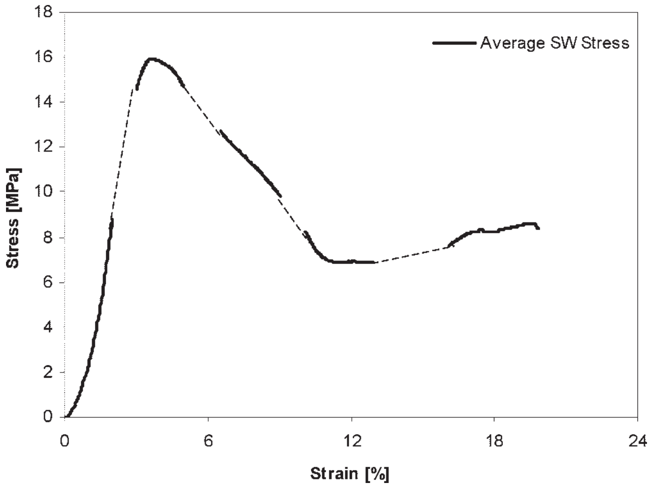

Figure 3. A sample data reconstruction to create a continuous stress-strain graph from a set of discrete curves.

The reconstructed raw data was then resampled and averaged to obtain stresses between 0 to 2% strain at intervals of 0.2% strain and between 2 to 20% strain at intervals of 1% strain. The data were used to determine statistical differences between the loads of the stepwise and continuous tests at corresponding strains and to determine the correlation between the stepwise and continuous loads. Modulus of elasticity, stiffness, yield strain and strength, ultimate strain and strength and ultimate load were calculated and statistical differences were assessed for the two loading regimens using a two-tailed Student *t* tests. Ultimate load and strain were defined as the initial peak load and its corresponding strain, respectively.

Microtomographic Imaging and Image Analysis

Progressive images were generated using a microtomographic imaging system (μCT 20, Scanco Medical, Bassersdorf, Switzerland), a compact fan-beam type tomograph, also referred to as desktop μCT.[30] This specific system with an isotropic spatial resolution of 28 μm has been used extensively for different research projects involving the assessment and analysis of microstructural bone and porous materials.

Measurements were stored in 3D image arrays with isotropic voxel sizes of 34 μm. A three-dimensional Gaussian filter with a filter width of 1.2 voxels, and a limited finite filter support of 1 voxel was used to suppress the noise in the volumes. In the next step, the cellular solid images were segmented from background using a global thresholding procedure.[31] Samples were binarized using thresholds that were 20.0 % of the maximum gray scale value for aluminum, 30.0 % for silicon carbide, 36.0 % for whale bone, and 14.0 % for human bone.

The 3D images of each compression step were combined into an animation, since 3D animations of testing experiments contribute significantly to the understanding of sample failure

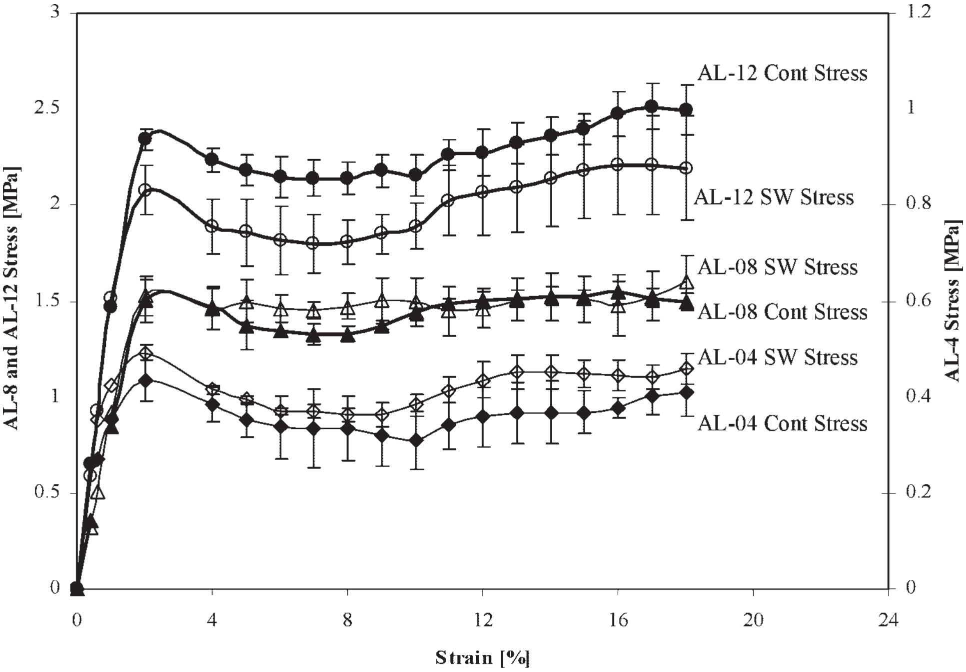

Figure 4. Stepwise and continuous stress-strain graphs for aluminum (AL-04, AL-08, AL-12) samples.

under load. For this purpose, the 3D images first had to be aligned with respect to the bottom end-plate, since this plate was considered to be fixed during the testing experiment. An algorithm was used to find the last plane of this end-plate in each 3D image enabling an alignment of the images along the perpendicular axis. A subsequent 2D correlation procedure was used in the first five sample planes in order to perform the alignment. These aligned images were then all visualized under the same conditions (orientation, light settings) using the Marching Cubes algorithm[32] and the resulting images were finally turned into an animation.

RESULTS

Aluminum Foam

The stress-strain curves between the stepwise and continuous testing methods showed identical pre-2% strain regions for all AL-04, AL-08, and AL-12 samples. As for the post-yield portions of the graphs, the AL-04 stepwise curve was overestimated by roughly 4%, the AL-08 stepwise curve was nearly identical to the continuous one, and, finally, the AL-12 stepwise curve was underestimated by roughly 7% (Figure 4). A regression analysis between the stepwise and the continuous stress data for all density groups was performed to further analyze the correlation between the stress-strain curves of both testing methods. This analysis revealed coefficient of determination (r^2) values of 0.97 for AL-04 and 0.98 for AL-08 and AL-12 samples, suggesting a high degree of correlation between the stepwise and continuous stress-strain curves. In addition, there were no significant differences observed between the continuous and stepwise testing mechanical properties ($p > 0.05$) (Table II).

The results from the 8% volume density aluminum foam continuous tests were compared to results obtained by Bart-Smith et al.,[33] who performed compression tests on 8% volume density ERG aluminum foam samples (size 30 × 30 × 50 mm). In that study, the samples were loaded from 0 to 20% strain with a strain rate of 0.050 mm/s using an Instron 8511 mechanical testing device (Instron Corp., Canton, MA). The mechanical properties obtained from these tests are reflected in Table III. Ultimate strength values were identical, and the reported average yield strength value for the MTDAQ continuous test was within 4% of the results reported by Bart-Smith et al. (within the standard deviation of the test). The visual data obtained from the application of stepwise microcompression in combination with time-lapsed μCT on AL-04 foam samples are demonstrated in Figure 6(A). The relatively homogenous distribution of aluminum rods and plates shows a pattern of failure consistent with a band of failure at the lower end of the sample, with the remainder of the sample remaining relatively intact. The "snapshots" of progressive strain steps applied to the sample reveal the actual failure mode of the microarchitectural elements comprising the sample, in addition to revealing the overall failure mechanism of the sample.

Silicon Carbide Foam

The SiC foam stress-strain curves contained all the classical characterizations of a brittle material with the sharply increasing elastic region followed by the catastrophic failure at the ultimate strength point. In addition, the points of yield and ultimate failure coincide due to the sharp failure properties of the constituent material.

There was no significant difference between the mechanical properties obtained from the continuous and stepwise

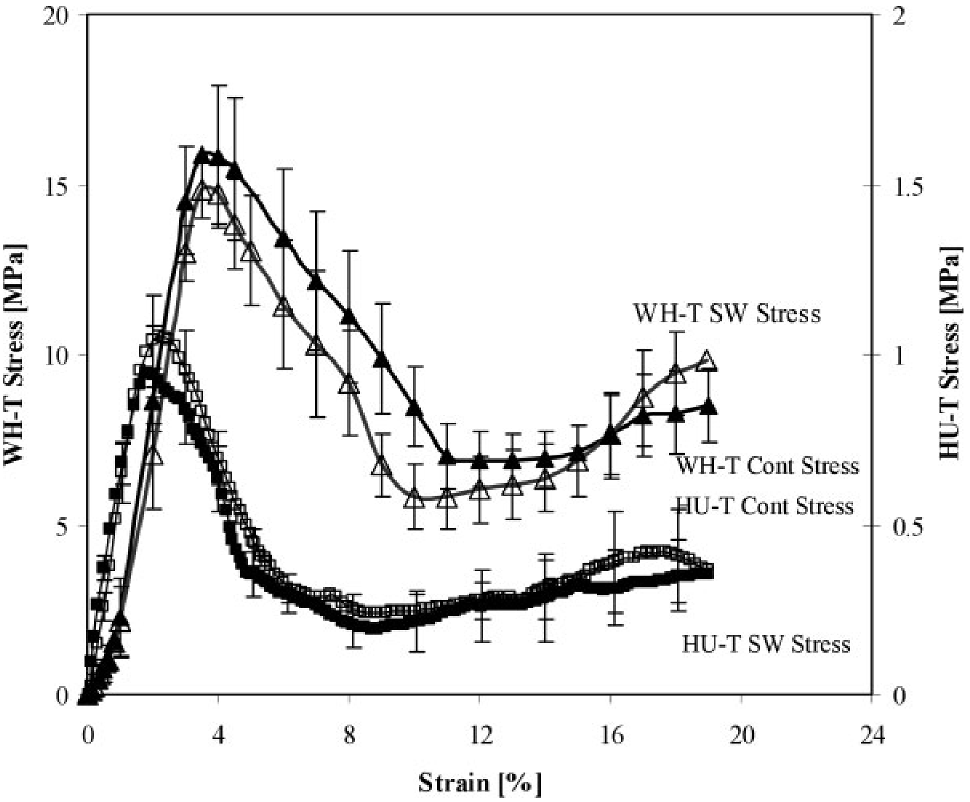

Figure 5. Stepwise and continuous stress-strain graphs for whale (WH-T) and human (HU-T) samples. Left vertical ordinate shows the stress for the WH-T group, and the right vertical ordinate shows the stress for the HU-T group.

testing methods ($p > 0.05$) (Table IV). Using cellular solids relationships for open cell foam materials, the compressive strength and modulus of elasticity values of the SiC foam properties were calculated based on the following equations:

$$\sigma_Y \approx 0.65 \cdot \sigma_s \cdot \rho^{3/2} \qquad (1)$$

$$E_Y \approx E_s \cdot \rho^2 \qquad (2)$$

where σ_Y is the compressive strength of the open cell foam, σs is the compressive strength and E_s is the modulus of elasticity of the cell wall property (Silicon Carbide), and ρ is the relative density of the foam (10%). The compressive

TABLE II. Mechanical Properties of All Stepwise (SW) and Continuous (Cont) Aluminum Foam Samples (AL-04, AL-08, and AL-12)

		Apparent Density [kg/m3]	Yield Strength [MPa]	Yield Strain [%]	Ultimate Strength [MPa]	Ultimate Strain [%]	Mod. of Elasticity [MPa]	Ultimate Load [N]	Stiffness [N/m]
AL-04	Cont.	0.12	0.41	1.04	0.48	1.93	67.30	22.67	197.00
	Std. Dev.	0.003	0.09	0.58	0.14	1.21	11.30	6.73	40.40
	SW	0.12	0.39	0.78	0.51	2.16	68.50	24.29	207.70
	Std. Dev.	0.003	0.02	0.07	0.01	0.44	9.40	0.73	25.50
	p value	0.60	0.45	0.40	0.88	0.64	0.81	0.86	0.77
AL-08	Cont.	0.226	1.48	1.77	1.64	2.71	121.40	75.65	352.20
	Std. Dev.	0.008	0.10	0.46	0.07	0.36	17.80	5.85	44.90
	SW	0.23	1.50	1.73	1.64	2.39	127.60	72.97	357.60
	Std. Dev.	0.01	0.08	0.61	0.09	0.42	20.70	2.18	53.20
	p value	0.99	0.80	0.72	0.55	0.18	0.41	0.52	0.38
AL-12	Cont.	0.29	2.23	1.69	2.44	2.76	182.90	113.24	534.00
	Std. Dev.	0.01	0.32	0.24	0.22	0.36	16.90	14.30	54.90
	SW	0.29	1.90	1.38	2.11	2.24	185.40	98.22	563.60
	Std. Dev.	0.02	0.39	0.36	0.38	0.44	56.50	14.60	162.70
	p value	0.94	0.17	0.15	0.12	0.07	0.93	0.14	0.71

TABLE III. Comparison of AL-08 and SiC MTDAQ Continuous Mechanical Properties with Literature

	Test	Yield Strength [MPa]	Standard Dev.	Ultimate Strength [MPa]	Standard Dev.
Comparison of mechanical properties of continuous AL-08 MTDAQ tests with those reported by Bart-Smith et al.[33]					
AL-08	Cont. MTDAQ	**1.48**	*0.10*	**1.64**	*0.07*
	Bart-Smith et al.	**1.42**	—	**1.64**	—
Comparison of mechanical properties of continuous SiC MTDAQ tests with those calculated using cellular solid relationships for open cells.					
SiC	Cont. MTDAQ	**21.95**	*2.27*	**4.25E+03**	*7.90E+02*
	Open Cell Rel.	**21.99**	—	**4.61E+03**	—

strength of Silicon carbide is 1.07 GPa, and its modulus of elasticity is 461 GPa. The results obtained from the above equations in comparison with values obtained from the MTDAQ continuous stress-strain tests are illustrated in Table III, where the values obtained from these relationships were within the range and standard deviation of those obtained through the MTDAQ continuous stress-strain tests ($p > 0.05$). The visual data obtained from the application of stepwise microcompression in combination with time-lapsed μCT on SiC samples are demonstrated in Figure 6(B). The brittle nature of the SiC foam material is demonstrated by the catastrophic failure of the above-mentioned sample early on in the compression process, immediately followed by the filling phase.

Whale Cancellous Bone

The stress-strain curves between the stepwise and continuous testing methods showed almost identical pre-2% strain regions for all WH-T samples. There was a trend of underestimation of up to 5% observed at the postfailure region of the stepwise curve. This trend continued on until the 15% strain

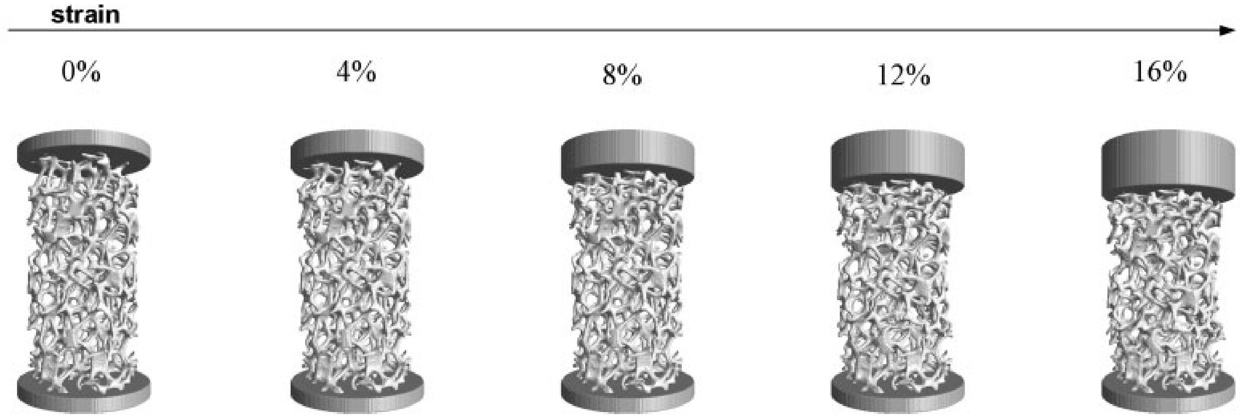

A – Aluminum foam core

B – Silicon carbide core

Figure 6. Image-guided failure assessment of representative (A) aluminum foam (AL-08) and (B) silicon carbide foam (SiC). Time-lapsed microcompression steps of 0, 4, 8, 12, and 16% strain are illustrated sequentially from left to right.

TABLE IV. Mechanical Properties of All Stepwise (SW) and Continuous (Cont) Silicon Carbide Foam Samples (SiC)

		Yield Strength [MPa]	Yield Strain [%]	Ultimate Strength [MPa]	Ultimate Strain [%]	Mod. of Elasticity [MPa]	Ultimate Load [N]	Stiffness [N/m]
SiC	Cont.	21.95	2.93	21.94	2.93	4.25	186.34	728.90
	Std. Dev.	2.27	0.44	2.272	0.44	0.79	19.30	135.30
	SW	20.84	2.87	20.84	2.87	4.15	174.44	711.57
	Std. Dev.	1.51	0.21	1.51	0.21	0.38	11.95	57.16
	p value	0.40	0.88	0.44	0.88	0.87	0.34	0.95

level and from then on gave way to a trend of overestimation for the stepwise stress-strain curve (Figure 4). Also, the negative slopes of both stepwise and continuous tests were almost identical. The regression analysis between the stepwise and the continuous stress data revealed a coefficient of determination (r^2) value of 0.96, suggesting a high degree of correlation between the stepwise and continuous stress-strain curves. In addition, there was no significant difference between the mechanical properties obtained from the continuous and stepwise testing methods ($p > 0.05$) (Table V). The visual data obtained from the application of stepwise microcompression in combination with time-lapsed μCT on WH-T samples is demonstrated in Figure 7(A). The highly platelike structure of the WH-T sample has resulted in a bandlike failure in the mid-section of the sample, where the platelike elements demonstrate mostly bending failure, while the overall sample demonstrates a buckling type failure mechanism.

Human Cancellous Bone

The stress–strain curves between the stepwise and continuous testing methods showed almost identical pre-2% strain regions for all HU-T samples. The post-yield behavior of the stepwise stress-strain curve was nearly identical to the continuous one, including near identical negatives slopes between the two testing methods (Figure 4). The regression analysis between the stepwise and the continuous stress data revealed a coefficient of determination (r^2) value of 0.98, suggesting a high degree of correlation between the stepwise and continuous stress-strain curves. In addition, there was no significant difference between the mechanical properties obtained from the continuous and stepwise testing methods ($p > 0.05$) (Table V). The visual data obtained from the application of stepwise microcompression in combination with time-lapsed μCT on HU-T samples is demonstrated in Figure 7(B, C). A combination of barreling and buckling failure modes are observed in a band in the mid to lower section of the sample in the full and slices views, where the top portion of the sample remains relatively intact. It is noteworthy to observe the bending failure of the individual rodlike and platelike elements in the region of failure, with the elements bending from 10 to more than 150°. Despite very high bending angles, the trabecular elements show remarkable ductility where trabeculae will not disconnect well beyond the yield strain of roughly 1–2%. In other words, they bend to the limit yet resist breaking due to the presence of the very compliant organic matrix.

Average Strain and Axial Divergence in All Samples

For all samples, the average divergence (in parentheses) between the nominal and measured strain steps for all tests, as obtained from the height the specimen in μCT imaging at each strain step, in comparison to the nominal values, were as

TABLE V. Mechanical Properties of All SW and Cont Biological Specimens

	Apparent Density [kg/m3]	Yield Strength [MPa]	Yield Strain [%]	Ultimate Strength [MPa]	Ultimate Strain [%]	Mod. of Elasticity [MPa]	Ultimate Load [N]	Stiffness [N/m]
Mechanical properties of all step-wise (SW) and continuous (Cont) whale cancellous bone samples (WH-T)								
WH-T								
Cont.	1.29	14.96	3.01	16.11	3.69	738.80	781.20	2198.50
Std. Dev.	0.07	4.08	0.62	3.65	0.33	107.50	207.90	367.90
SW	1.27	15.15	3.01	16.18	3.43	693.70	797.80	2097.70
Std. Dev.	0.04	4.35	0.55	4.47	0.31	158.60	255.10	547.70
p value	0.52	0.93	0.99	0.97	0.12	0.56	0.90	0.71
Mechanical properties of all step-wise (SW) and continuous (Cont) human vertebral cancellous bone foam samples (HU-T).								
HU-T								
Cont.	3.87E-04	1.04	1.86	1.08	2.17	65.41	53.47	273.90
Std. Dev.	1.22E-04	0.37	0.11	0.37	0.20	23.71	19.68	105.40
SW	3.73E-04	0.97	1.72	1.023	2.01	63.38	50.52	268.50
Std. Dev.	1.21E-04	0.32	0.59	0.31	0.57	11.04	15.36	47.10
p value	0.96	0.61	0.95	0.59	0.95	0.52	0.56	0.54

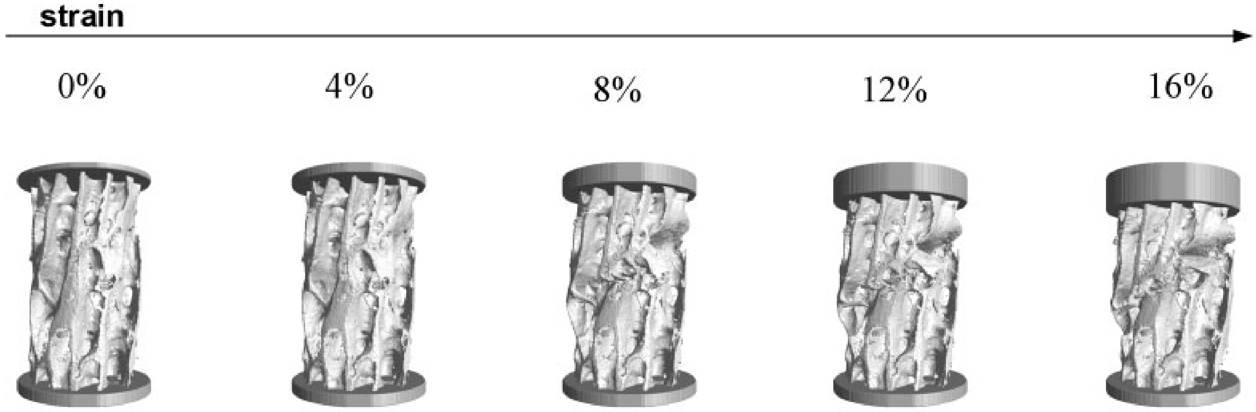

A - Whale trabecular bone core

B – Male Lumbar Region (L5) trabecular bone core – Full view

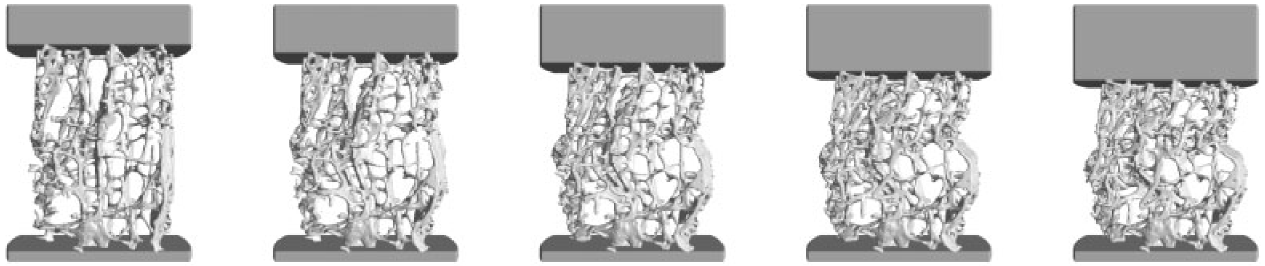

C - Male Lumbar Region (L5) trabecular bone core – Sliced view

Figure 7. Image-guided failure assessment of representative (A) whale cancellous bone (WH-T); (B) full sample view, human cancellous bone (HU-T) samples; and (C) sliced sample view, human cancellous bone samples. Time-lapsed microcompression steps of 0, 4, 8, 12, and 16% strain are illustrated sequentially from left to right.

follows: for 2% (0.44%), for 4% (0.67%), for 8% (0.40%) for 12% (0.18%), for 16% (0.21%), and for 20% (0.58%); and the correlation between these two strain measurements was excellent ($r^2 = 1.0$). Additionally, the average divergence of the sample axis from the predominant direction of the eigenvectors was 1.0° to 5.0° for all samples.

DISCUSSION

The first goal of this project was to design and fabricate a novel micromechanical testing system capable of accurately collecting the mechanical and visual failure properties of cellular solids, and, second, to observe failure behaviors of various cellular solids in order to gain insight into failure modalities involved with those solids in relation to their structural/material characteristics. With respect to the first aim, a new versatile microcompression testing system for time-lapsed imaging of sample failure was designed and successfully implemented. The slight variation in the results for the AL-08 continuous tests from those obtained by Bart-Smith et al.[33] is attributed to the fact that the open cell yield strength equation is designed for samples with at least 8 cell lengths in each direction, a condition met by the study performed by Bart-Smith et al. and not met by our study due to the spatial restriction of the micro-CT bore. In addition, the mechanical properties from the SiC continuous tests were similar to those obtained from cellular solid relationships for open cell foam materials (the results from cellular solid relationships were within the range and SD of the results obtained from continuous SiC tests).

The stress-strain curves between the stepwise and continuous testing methods showed almost identical elastic regions for all WH-T and HU-T samples. The high coefficient of determination for the regression analysis between the two curves, coupled with similar mechanical results ($p > 0.05$) obtained from the two testing methods suggest that the results obtained from the stepwise method are validated by the gold standard classical continuous tests to provide mechanical and visual information of the behavior of whale and human cancellous bone samples. These findings clearly show that stepwise microcompression is a valid technique to study the structural failure mechanism in cellular solids from a mechanical and visual point of view.

With respect to the second aim, the advantage of this system is elucidated best by the animations generated from the sequential μCT images (http://www.bioelectronics.ethz.ch/mtdaq), where the failure process is clearly highlighted. These animations and the sequential images shown in Figures 6 and 7 outline a specific failure mode observed in all cellular solid samples tested for this study. In general, failure in all samples occurred in a bandlike failure with the remaining portions of the samples remaining relatively intact. In Figure 6(A), a horizontal band of failure is observed at the lower part of the sample, where individual elements fail in buckling and bending modes. However, the top 70% of the sample is remarkably intact through all strain steps. The isotropic nature of the sample under compressive loading has resulted in a horizontal band of failure (much like those observed in controlled implosion of buildings), where the weakest subregion has taken the brunt of the force and collapsed under load. Figure 6(B) shows the catastrophic failure of the SiC sample starting very early on in the compression process due to the brittleness of the SiC material. A sharp angular band of failure is observed from the top right of the sample extending to the bottom left. The bands of failure for the whale and human samples are manifested in different modes due to the structural differences observed in the two. The platelike structure of the whale sample has resulted in bending of the vertical plate elements at an almost 45° angle (much like shear behavior) with an overall buckling effect for the entire sample, whereas for the human sample, which is mainly comprised of rods, very large angular deformations (bending) are observed in most rods with an overall barreling effect for the entire sample. Contrary to the SiC samples, the ductile nature of bone tissue (presence of collagen) has enabled the individual plates and rods to bend in a range of 10° to 150° without actual disconnection. Evidenced by these observations, individual trabecular elements seem to undergo much higher strain levels than those applied externally highlighting the need for further assessment of the mechanical behavior of trabecular bone in the postfailure (plastic) region. This statement runs contrary to the existing notion that bone ultimately fails at 1% external strain, as we see trabecular elements maintaining their union under much larger strains. It must be noted though that the mineralized phase of the bone has failed or even fractured at this point; nevertheless, the organic phase (mostly collagen) is keeping the trabeculae together. This provides an important biological advantage in terms of the bone's capacity to heal, i.e., it is much simpler to "remineralize" a microfracture (typically a microcallus is formed) than to reconnect fully disconnected fractured trabeculae. On the other hand, bandlike failure of samples suggests that strain levels are generally underreported (L_0 being the initial length of the entire specimen as opposed to the initial length of the band of failure), hence directly affecting the modulus of elasticity values in bone samples.

The μCT images were taken using a Scanco μCT 20 imaging system. Currently, Scanco μCT 40 systems can produce better images at roughly 1/10th of the time. So, with the advances made in the field of μCT imaging, scan times and resolution of the images can be optimized. However, the 36-μm resolution imaging in this study seems to be adequate for the study (relative size of human trabeculae 150–250 μm). Nevertheless, it should be noted that although the methods presented in this article were originally developed for X-ray tomographic imaging, they are also applicable to other 3D imaging modalities. Especially, magnetic resonance microscopic imaging (μMRI) may have considerable potential providing 3D information with isotropic voxel resolutions of roughly 50 to 150 μm fully noninvasively and without ionization.[34]

Further improvements in imaging time and resolution, coupled with addition of corrections for the system's load frame compliance, will produce even better results for this testing modality.

In conclusion, the MTDAQ and the redesigned MCD-II form a unique microcompression testing system that in combination with 3D microcomputed tomography allows visualization of failure initiation and propagation in a noninvasive way in cellular solids. The nature of this screw-driven system, with a rotating end-effector that moves in the axial direction and locks the applied displacement to the specimen, makes the system unique and not reproducible in a standard hydraulic or screw-driven mechanical testing system. The clear advantage of this system lies in its capability to provide both mechanical and visual data on a specimen under load, something not accomplished by a standard mechanical testing system. Additionally, image-guided failure assessment is quite laborious and occupies a mechanical testing system quite heavily. Cost of standard multipurpose testing systems is high compared to a simpler stand-alone system as introduced here. Therefore, this approach complements the conventional mechanical testing methods by giving visual insight, in the form of actual failure animations, into the failure mechanisms of cellular solids. This area is of particular interest for bone research, where the microstructure and the mechanical behavior of trabecular bone is used extensively as an assay to monitor progression and regression of bone-related diseases and treatment options due to the high metabolic rate of trabecular bone.

We acknowledge Dr. Brian Snyder from the Orthopedic Biomechanics Laboratory for his helpful comments and suggestions. Our sincere gratitude is extended to the members of the Scientific Instrument Facility at Boston University's Department of Physics for their valuable help during the manufacturing and operational phase of the project. The authors also acknowledge the reviewer for the insightful comments that were incorporated into this manuscript.

REFERENCES

1. Silva MJ, Gibson LJ. Modeling the mechanical behavior of vertebral trabecular bone: effects of age-related changes in microstructure. Bone 1997;21:191–199.
2. Williams JL, Lewis JL. Properties and an anisotropic model of cancellous bone from the proximal tibial epiphysis. J Biomech Eng 1982;104:50–56.
3. Jensen KS, Mosekilde L. A model of vertebral trabecular bone architecture and its mechanical properties. Bone 1990;11:417–423.
4. Gibson LJ. The mechanical behaviour of cancellous bone. J Biomech 1985;18:317–328.
5. Guo XE, Kim CH. Mechanical consequence of trabecular bone loss and its treatment: a three-dimensional model simulation. Bone 2002;30:404–411.
6. Kasra M, Grynpas MD. Static and dynamic finite element analyses of an idealized structural model of vertebral trabecular bone. J Biomech Eng 1998;120:267–272.
7. Hollister SJ, Fyhrie DP, Jepsen KJ, Goldstein SA. Application of homogenization theory to the study of trabecular bone mechanics. J Biomech 1991;24:825–839.
8. Pugh JW, Rose RM, Radin EL. A possible mechanism of Wolff's law: trabecular microfractures. Arch Int Physiol Biochim 1973;81:27–40.
9. Townsend PR, Rose RM, Radin EL. Buckling studies of single human trabeculae. J Biomech 1975;8:199–201.
10. Beaupre GS, Hayes WC. Finite element analysis of a three-dimensional open-celled model for trabecular bone. J Biomech Eng 1985;107:249–256.
11. Kim HS, Al-Hassani ST. A morphological model of vertebral trabecular bone. J Biomech 2002;35:1101–1114.
12. Ruimerman R, van Rietbergen B, Hibers P, Huiskes R. A 3-dimensional computer model to simulate trabecular bone metabolism. Biorheology 2003;40:315–320.
13. Gibson LJ, Ashby MF. Cellular solids. Cambridge University Press: New York: 1997.
14. Linde F, Norgaard P, Hvid I, Odgaard A, Soballe K. Mechanical properties of trabecular bone. Dependency on strain rate. J Biomech 1991;24:803–809.
15. Dalle Carbonare L, Giannini S. Bone microarchitecture as an important determinant of bone strength. J Endocrinol Invest 2004;27:99–105.
16. Forwood MR. Mechanical effects on the skeleton: are there clinical implications? Osteoporos Int 2001;12:77–83.
17. Jiang C, Giger ML, Kwak SM, Chinander MR, Martell JM, Favus MJ. Normalized BMD as a predictor of bone strength. Acad Radiol 2000;7:33–39.
18. Oden ZM, Selvitelli DM, Hayes WC, Myers ER. The effect of trabecular structure on DXA-based predictions of bovine bone failure. Calcif Tissue Int 1998;63:67–73.
19. Ciarelli MJ, Goldstein SA, Kuhn JL, Cody DD, Brown MB. Evaluation of orthogonal mechanical properties and density of human trabecular bone from the major metaphyseal regions with materials testing and computed tomography. J Orthop Res 1991;9:674–682.
20. Choi K, Goldstein SA. A comparison of the fatigue behavior of human trabecular and cortical bone tissue. J Biomech 1992;25: 1371–1381.
21. Crowell RR, Shea M, Edwards T, Clothiaux PL, White AA, Hayes WC. Cervical injuries under flexion and compression loading. J Spinal Disord, 1993;6:175–181.
22. Michel MC, Guo XE, Gibson LJ, McMahon TA, Hayes WC. Compressive fatigue behavior of bovine trabecular bone. J Biomech 1993;26:453–463.
23. Norrdin RW, Kawcak CE, Capwell BA, McIlwraith CW. Subchondral bone failure in an equine model of overload arthrosis. Bone 1998;22:133–139.
24. Muller R, Gerber SC, Hayes WC. Micro-compression: a novel technique for the nondestructive assessment of local bone failure. Technol Health Care 1998;6:433–444.
25. Nazarian A, Muller R. Time-lapsed microstructural imaging of bone failure behavior. J Biomech 2004;37:55–65.
26. Deutschman AD, Wilson MW. Machine design, theory and practice. New York: McMillan. 1975.
27. Keaveny TM, Borchers RE, Gibson LJ, Hayes WC. Trabecular bone modulus and strength can depend on specimen geometry. J Biomech 1993;26:991–1000.
28. Keaveny TM, Borchers RE, Gibson LJ, Hayes WC. Theoretical analysis of the experimental artifact in trabecular bone compressive modulus. J Biomech 1993;26:599–607.
29. Keaveny TM, Wachtel EF, Ford CM, Hayes WC. Differences between the tensile and compressive strengths of bovine tibial trabecular bone depend on modulus. J Biomech 1994;27:1137–1146.
30. Ruegsegger P, Koller B, Muller R. A microtomographic system for the nondestructive evaluation of bone architecture. Calcif Tissue Int 1996;58:24–29.
31. Muller R, Ruegsegger P. Micro-tomographic imaging for the nondestructive evaluation of trabecular bone architecture. Stud Health Technol Inform 1997;40:61–79.
32. Lorensen WE, Cline HE. Marching cubes: a high resolution 3D surface construction algorithm. Comput Graph 1987;21:163–169.
33. Bart-Smith H, Bastawros AF, Mumm DR, Evans AG, Sypeck DJ, Wadley HNG. Deformation and yielding mechanisms in cellular Al alloys determined using X-ray tomography and surface strain mapping. Acta Mater 1998;46:3583–3592.
34. Weierstall U, Chen Q, Spence JCH, Howells MR, Isaacson M, Panepucci RR. Image reconstruction from electron and X-ray diffraction patterns using iterative algorithms: experiment and simulation. Ultramicroscopy 2002;90:171–195.